Effects of heat transfer on transitional states of supersonic boundary layers

By M. S. Shadloo†, A. Hadjadj†, D. J. Bodony‡, F. Hussain†† AND S. K. Lele

Through high-resolution simulations, the present study aims to investigate several laminar-to-turbulent transition scenarios in the presence of wall-heat transfer for supersonic boundary layers over strongly heated/cooled and adiabatic flat plates. The laminar boundary layer is tripped using a suction and blowing technique with a single-frequency, multiple-spanwise wavenumber excitation. The results are evaluated and compared to linear stability theory in order to isolate the effect of wall-heat transfer, as well as forcing parameters, on the transition. It was found that increasing the disturbance amplitude as well as perturbation frequency moves the transition upstream. Also, the effect of wall heating was seen to stabilize the flow and to postpone the transition, contrary to the wall cooling.

1. Background and motivation

The transition from laminar flow to turbulent flow in boundary layers, such as on flat plates or swept wings, may be caused by small-amplitude perturbations that grow as they propagate downstream. These perturbations are commonly analyzed using spatial linear stability theory (LST) in order to obtain their respective growth rate and amplification. Experimental observations show that the mechanism of laminar-turbulent transition (LTT) in boundary layers is sensitive to the presence of internal and external perturbations (Matsubara & Alfredsson 2001). Boundary layer transition is classified into orderly and bypass transitions. While the former is generally characterized by the amplification of linear waves, such as Tollmien-Schlichting (TS), the definition of the latter is less precise but commonly used to describe transition beneath vortical disturbances (Durbin & Wu 2007) and other non-modal transition scenarios. The initial stage of the bypass transition may also be induced by the amplification of streamwise-elongated disturbances to reach a comparable amplitude as the free-stream turbulence intensity. This process is followed by the creation of low-speed streaks that become unstable, due to continuous free-stream turbulent forcing (Schoppa & Hussain 2002), and locally break down into turbulent spots (Jacobs & Durbin 2001).

Klebanoff (1971) was the first to identify the appearance of streamwise-elongated streaks in laminar boundary layers caused by free-stream turbulence. Arnal & Juillen (1978) demonstrated that for levels of free-stream disturbances generally higher than 1%, the dominant low-frequency distortions differ from the TS waves. Later, Kendall (1985) denoted them Klebanoff modes. Since then, several researchers attempted to investigate numerically different possible scenarios to address LTT mechanisms and their active modes caused by low-frequency disturbances using direct numerical simulation (DNS) for a wide range of problem parameters (Jacobs & Durbin 2001; Wu & Moin

† INSA of Rouen, France
‡ Department of Mechanical Engineering, University of Illinois at Urbana-Champaign
†† Department of Mechanical Engineering, Texas Tech. University

2010). Concerning high-speed boundary layer transitions, a few DNS studies have been conducted by De Tullio *et al.* (2013) and Ryu *et al.* (2015), but they were mainly focused on bypass transition caused by an isolated or a series of roughness elements. Several parameters, such as roughness shape, height, and width, as well as flow properties (Mach and Reynolds numbers), have been investigated in both supersonic and hypersonic regimes. Their objective was to better understand the space-time transition occurrence, its physical nature and the main driving mechanisms. However, such phenomena are still poorly understood even when compared to low-speed flows. An extensive review on the current state of the art of LTT in high-speed flows can be found in Schneider (2008).

Although similarities between low- and high-speed flows in LTT mechanisms have been reported (Redford *et al.* 2010; Bernardini *et al.* 2012), the compressibility effects are absent in the former. In the latter, in addition to its generation at the wall, vorticity can be created through baroclinicity. This effect can be pronounced either in hypersonic Mach numbers or in the presence of wall-heat transfer. Few have considered the joint effects of high Mach number and wall temperature on roughness-induced bypass transition (Redford *et al.* 2010; Bernardini *et al.* 2012). For instance, Redford *et al.* (2010) found that the critical Reynolds number based on roughness height for transition is higher for cold walls. They also found that the wall temperature plays a secondary role at high Mach numbers, with cooled walls having lower lateral growth rate in the evolution of turbulent spots.

However, DNS data of LTT with wall-heat transfer are nearly absent in the literature (with some exception for hypersonic flows, see for instance Franko & Lele (2013)). It is noted that a change in the wall temperature causes significant changes in the boundary layer properties. Studying the effect of wall-heat transfer in LTT is therefore crucial, especially for high-speed flows. The current study focuses on the use of DNS to study receptivity and transition mechanisms occurring in supersonic wall-bounded flows subjected to strong heat transfer at the wall.

2. Numerical procedure

2.1. *Numerical method used in DNS*

This work relies on a well-validated DNS and LES research code, CHOC-WAVES, that solves the fully three-dimensional, compressible, unsteady Navier-Stokes equations for a perfect gas. The convective fluxes are discretized by means of a hybrid conservative sixth-order-central/fifth-order weighted essential non-oscillatory (WENO) scheme. To improve numerical stability, the convective terms are split in a skew-symmetric form in order to minimize the aliasing error and enforce discrete conservation of the kinetic energy. The diffusive terms are expanded in Laplacian form and are approximated with fourth- or sixth-order formulas. The system of equations is integrated in time using a third-order Runge-Kutta scheme. More details regarding the numerical solver and its validation can be found in Chaudhuri *et al.* (2011*a*,*b*), Shadloo *et al.* (2014, 2015) and Ben-Nasr *et al.* (2016).

2.2. *Problem setup*

In this study, a transition occurring at $\mathrm{M}_\infty = 2.2$ over a flat plate is considered. The free-stream temperature and pressure are $T_\infty = 177\,\mathrm{K}$ and $p_\infty = 23796\,\mathrm{Pa}$, respectively, and the Prandtl number is $\mathrm{Pr} = 0.72$. Velocity, temperature and density profiles at the inlet (see Figure 1) are calculated using a dedicated solver to obtain similarity solutions

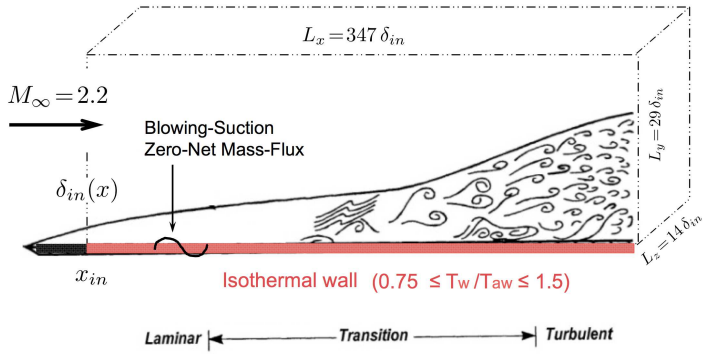

FIGURE 1. Schematic of computational domain and boundary conditions. The used inflow parameters are $\mathrm{Re}_{x,in} = u_\infty\, x_{in}/\nu_\infty = 2.34 \times 10^6$, $\mathrm{Re}_{\delta,in} = u_\infty\, \delta_{in}/\nu_\infty = 9944$ and $\mathrm{Re}_{\theta,in} = u_\infty\, \theta_{in}/\nu_\infty = 907$, where $u_\infty = 587$ m/s is the free-stream velocity, $\delta_{in} = 0.43$ mm and $\theta_{in} = 0.09\,\delta_{in}$ are the inlet boundary layer and momentum thicknesses, respectively.

of a laminar compressible boundary layer over an adiabatic flat plate. Although all test cases considered have the same inflow and initial conditions, which correspond to those of adiabatic laminar flow, the thermal boundary condition at the wall is different for each case. This condition is applied at a given distance x_{in}, which is the location of the inlet boundary where the similarity solution is applied. For the adiabatic case, the wall temperature is kept at $T_w = T_{aw}$, while for the cooled and heated cases the temperature is maintained at $T_w = 0.75\,T_{aw}$ and $T_w = 1.5\,T_{aw}$, respectively, with $T_{aw} \approx 1.82\,T_\infty$. The fluid is considered as air with constant specific heats. The viscosity is calculated using Sutherland's law.

The computational domain, shown in Figure 1, is set up large enough (i.e. $L_x/\delta_{in} \approx 347$) to cover both the transition and the fully turbulent regions in most of the cases. The domain height and width are chosen such that the flow features are not influenced by the wall-normal outflow and spanwise periodic boundary conditions (i.e., $L_y/\delta_{in} \approx 29$ and $L_z/\delta_{in} \approx 14$). It is noted that this choice leads to almost the same computational height and to an approximately 30% larger domain in both streamwise and spanwise directions as in Pirozzoli *et al.* (2004).

Other boundary conditions are those of supersonic inflow/outflow conditions at the upstream ($x_1 = x_{in}$) and downstream ($x_N = x_{in} + L_x$) of the computational domain, respectively. At the wall, i.e., $y = 0$, the no-slip boundary condition is imposed except in the narrow strip between $x_a = x_{in} + 0.3\,\delta_{in}$ and $x_b = x_{in} + 0.6\,\delta_{in}$ where the disturbances are introduced. In this region, the wall-normal component of the velocity is prescribed by a single-frequency and multiple-spanwise wavenumber blowing and suction boundary condition as $v(x,z,t) = A\ f(x)\,[g(z)/max(g(z))]\,[h(t)/max(h(t))]$, where streamwise, spanwise and time-dependent variations are defined as $f(x) = 4\ \sin\theta(1-\cos\theta)/\sqrt{27}$, $g(z) = \sum_{l=1}^{l_{max}} Z_l \sin(2\pi l(z/L_z + \phi_l))$ and $h(t) = \sum_{m=1}^{m_{max}} T_m \sin(\omega t + \phi_m)$, with A and ω being the amplitude and the fundamental frequency of the disturbance, respectively. Here, $\theta = 2\pi(x - x_a)/(x_b - x_a)$, and ϕ_l and ϕ_m are random numbers ranging from 0 to 1. Additionally, $\sum_{l=1}^{l_{max}} Z_l = 1$, $Z_l = 1.25 Z_{l+1}$, for $l_{max} = 20$ and $\sum_{m=1}^{m_{max}} T_m = 1$, $T_m = 1.25 T_{m+1}$, for $m_{max} = 20$. It is noted that this method is a modified version of that introduced in Pirozzoli *et al.* (2004), which is able to induce transition.

Uniformly spaced mesh is used in both streamwise and spanwise directions with $N_x = 4096$ and $N_z = 320$, respectively. In the wall-normal direction, the total num-

Case	T_w/T_r	A/u_∞	ω (krad/s)	$\mathrm{Re}_{\theta,max}$	Δx^+	Δy^+_{min}	Δz^+
A1	1.0	0.040	75	3858	5.52	0.35	2.85
A2	1.0	0.024	150	3748	5.52	0.34	2.85
A3	1.0	0.024	75	2882	5.52	0.34	2.85
H1	1.5	0.040	75	3001	5.70	0.35	4.31
C1	0.75	0.040	75	4269	8.35	0.52	2.94

TABLE 1. Physical and computational parameters for different test cases. Subscripts *min* and *max* indicate the wall-normal spacing and the maximum achievable Reynolds number within the computational domain, respectively. Superscript + denotes the wall-unit normalization.

ber of mesh points is $N_y = 150$, clustered close to the wall using the function $L_y(1 + \tanh(\kappa_o y)/\tanh\kappa_o)$, with $\kappa_o \simeq 3$ as the grid stretching parameter. The computational parameters are listed in Table 1.

2.3. *Linear stability theory*

For the mean flow, the equations for a two-dimensional, compressible, laminar boundary layer are transformed into similarity coordinates according to the Levy-Lees transformed coordinates $\xi = \int \rho_\infty u_\infty \mu_\infty dx$ and $\eta = u_\infty/\sqrt{2\xi}\int \rho dy$. In these coordinates, continuity, momentum, and energy equations for a flat-plate boundary layer are reduced to a coupled system of ordinary differential equations. A shooting method, employing a fourth-order Runge-Kutta scheme and a Newton-Raphson iteration, is used to solve these equations simultaneously (Cebeci & Smith 1974).

It is assumed that the spatial and temporal evolution of the small disturbance q' follows the following propagating wave, $q'(x, y, z, t) = \hat{q}(y)\exp\{i(\alpha x + \beta z - \omega t)\}$, for real and positive frequency ω and spanwise wavenumber β. The streamwise wavenumber $\alpha = \alpha_r + i\alpha_i$ is generally complex valued. The real and imaginary parts of α are related to the phase velocity $c_{ph} = \omega/\alpha_r$ and the spatial growth rate $-\alpha_i$. Since the DNS uses periodic boundary conditions in the spanwise direction, the permissible spanwise wavenumbers are then $\beta^*_n = 2\pi n/L_z$, for $n \in \mathcal{Z}$, where $n = 1$ determines the smallest spanwise wavenumbers that the calculation permits. All other spanwise wavenumbers are integer harmonics of this lowest wavenumber.

3. Results and discussion

3.1. *Effect of disturbance amplitude and frequency*

To highlight the qualitative features of the transition, we focus on the effect of perturbation amplitude and frequency under the adiabatic wall condition. The reference case, A1, has the angular frequency and disturbance amplitude of $\omega = 75\,\mathrm{krad/s}$ and $A/u_\infty = 4\%$, respectively (see Table 1). For the A3 case, the perturbation amplitude is reduced to $A/u_\infty = 2.4\%$, while in the A2 case the angular frequency is increased by a factor of two (i.e. $A/u_\infty = 2.4\%$ and $\omega = 150\,\mathrm{krad/s}$).

As shown in Figure 2, a decrease in the perturbation amplitude causes a transition delay (comparing A3 with A1). However, an increase in the perturbation frequency promotes earlier transition upstream. This behavior is consistent with LST, as also depicted in Figure 2, where contours of the growth rate are expressed in terms of non-dimensional

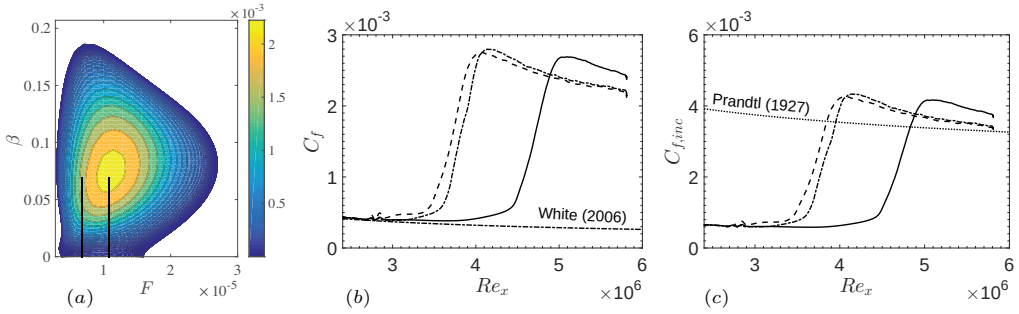

FIGURE 2. (a) Contours of LST growth rate in the frequency-spanwise wavenumber plane for $R_{in} = \sqrt{\mathrm{Re}_{x,in}} = 1527$. Vertical lines show non-dimensional values of two frequencies used in this study. (b) Compressible and (c) incompressible friction factor coefficients as a function of Re_x for A1 (dashed lines), A2 (dot-dashed lines) and A3 (solid lines) cases with adiabatic walls.

frequency, $F = \omega\nu_\infty/u_\infty^2$, and spanwise wavenumber, $\beta = \beta^* x/R$, with $R = \sqrt{\mathrm{Re}_x}$. For reference, the values of F and β for $\omega = 75$ krad/s and first spanwise mode are $F_{75} = 5.6 \times 10^{-6}$ and $\beta_1 = 0.069$, respectively. As can be seen, for these inflow and boundary conditions, doubling the perturbation frequency destabilizes the system toward the most unstable mode. Therefore, one may expect the transition process to grow faster in the streamwise direction and the appearance of the first turbulent spot to advance upstream.

Figure 2(b,c) illustrates the spatial evolution of the compressible and incompressible skin-friction coefficients. Upstream of the suction/blowing strip, all cases closely follow the correlation for the compressible flat-plate boundary layer, $C_{f,lam} = 0.664\,\vartheta_c\,\mathrm{Re}_x^{-0.5}$, where $\vartheta_c = \sqrt{(\rho_w/\rho_\infty)(\mu_w/\mu_\infty)}$ expresses the fluid density/viscosity variation. The value of C_f reaches a minimum at the streamwise position of the so-called transition location. It is then smoothly augmented, followed by a sharp increase. After experiencing an overshoot, the flow reaches the value that corresponds to a fully turbulent regime (i.e., $C_{f,inc} = 0.074\,\mathrm{Re}_x^{-0.2}$). Based on the aforementioned criterion, A1, A2 and A3 cases have the transition locations at $\mathrm{Re}_x \approx 2.9 \times 10^6$, $\mathrm{Re}_x \approx 3.1 \times 10^6$ and $\mathrm{Re}_x \approx 3.8 \times 10^6$, respectively. According to this criteria and comparing the streamwise position in the C_f curve, where the mean flow properties follow closely their turbulent counterpart, A1 and A3 have the shortest and largest transition regions, respectively. Additionally, it is found that the maxima in C_f have their highest and lowest values for A2 and A3, respectively. Therefore, one may conclude that the perturbation frequency and amplitude not only affect the transition length but also alter the maximum overshoot seen in the simulations. It is noted that such behavior was also reported by Sayadi *et al.* (2013) for different perturbation methods.

3.2. *Effect of wall-heat transfer*

To highlight the effect of wall-heat transfer on the transition process, we focus on the simulations with different isothermal wall conditions but at fixed perturbation amplitude and frequency (i.e., $A/u_\infty = 4\%$ and $\omega = 75$ krad/s). Compared to the adiabatic case (A1), the wall temperature is increased to $T_w/T_r = 1.5$ for the heated case (H1) and decreased to $T_w/T_r = 0.75$ for the cooled case (C1) case.

Snapshots of streamwise velocity in the streamwise-spanwise plane of these three cases at $y = 0.29\,\delta_{in}$ are illustrated in Figure 3. Streamwise-elongated streaks are visible in the

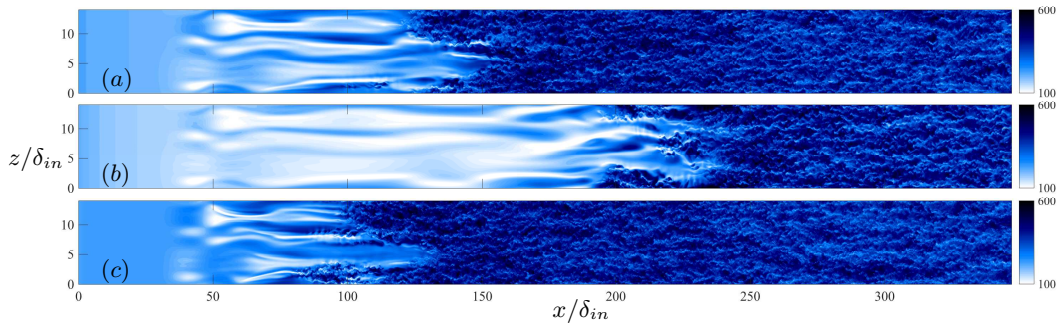

FIGURE 3. $x-z$ plane snapshots of the streamwise velocity component (m/s) for (a) adiabatic (A1), (b) heated (H1) and (c) cooled (C1) walls at $y/\delta_{in} = 0.29$.

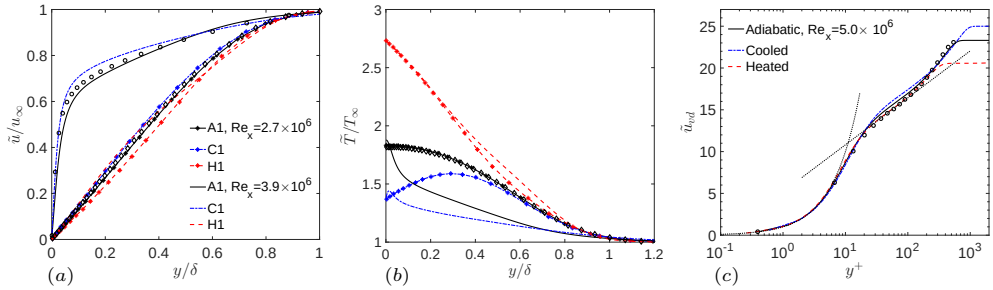

FIGURE 4. (a) Velocity, (b) temperature mean profiles and (c) Van-Driest transformed mean velocity for adiabatic (A1), heated (H1) and cooled (C1) cases; ∘, DNS by Shadloo *et al.* (2015) and ⋄, Blasius profile.

laminar and transitional regions. They become unstable, locally break down and create turbulent spots further downstream. It is found that the wall heating stabilizes the flow and postpones the transition.

As can be seen in Figure 4, the velocity profiles in the laminar stage ($\mathrm{Re}_x = 2.7{\times}10^6$) are actually quite close to each other and follow the Blasius profile. However, it is observed that the heated case does not transition by $\mathrm{Re}_x = 3.9\times10^6$, while the adiabatic and cooled cases become turbulent. As expected the mean temperature profiles are quite different between the adiabatic, heated and cooled cases even in the laminar stage. The corresponding effect on fluid density and viscosity affects the disturbance receptivity, linear instability and transition. The heated case has a substantial region of low-density fluid next to the wall, which with help from the increased viscosity of the fluid in the same near-wall region will significantly reduce the growth of disturbance energy and delays transition in the heated case. The opposite holds true for the cooling case.

Finally, close to the end of the computational domain, all cases exhibit fully turbulent flow. As shown in Figure 4(c), the viscous sublayer and logarithmic region are clearly recognizable in all cases. As expected, for this range of Reynolds numbers, the $-5/3$ slope is seen in the one-dimensional power spectrum for all cases, justifying aforementioned observation (see Figure 5). It is also noted that the oscillations seen in the laminar and transitional regions in Figure 4 correspond to sub-harmonic wavenumbers that are forced by the prescribed blowing and suction.

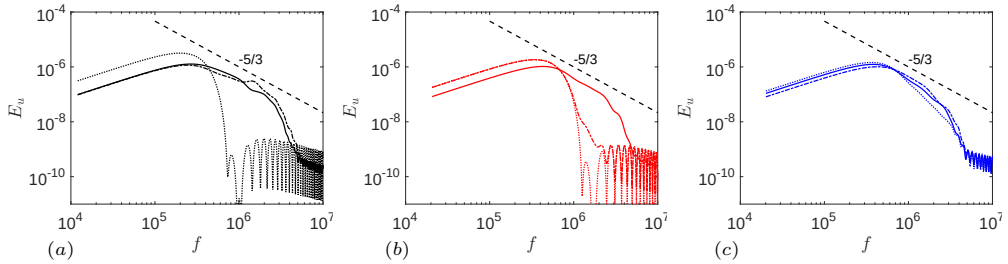

FIGURE 5. Normalized one-dimensional premultiplied frequency spectra of streamwise velocity fluctuation at $y/\delta_{in} = 0.29$ for different streamwise locations, namely, $\mathrm{Re}_x = 3.35{\times}10^6$, $4.36{\times}10^6$ and 5.37×10^6 for DNS with (a) adiabatic (A1), (b) heated (H1) and (c) cooled (C1) walls; $N_x = 3600$ (solid lines), $N_x = 2400$ (dot-dashed lines), $N_x = 1200$ (dotted lines).

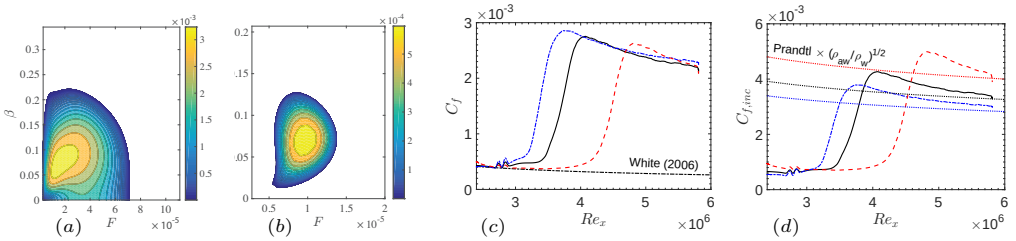

FIGURE 6. Contours of growth rate LST in the frequency-spanwise wavenumber plane at $R_{in} = \sqrt{\mathrm{Re}_{x,in}} \approx 1527$ for the cases with (a) heated and (b) cooled walls. (c) Compressible and (d) incompressible friction factor coefficients as a function of Re_x for DNS with —— adiabatic, - - - heated and — · — cooled walls.

It is worth mentioning that the latter observation contradicts with the LST prediction. As presented in Figure 6(a,b), according to the LST, the boundary layer instability region for the heated case expands and has higher growth rates, while it contracts and has lower growth rates when the boundary layer is cooled. The DNS results presented in Figure 6(c) clearly show that the transition starts at $\mathrm{Re}_x \approx 2.8\times10^6$, $\mathrm{Re}_x \approx 2.9\times10^6$ and $\mathrm{Re}_x \approx 3.7\times10^6$ for the cooled (C1), adiabatic (A1) and heated (H1) walls, respectively, based on the minimum skin-friction coefficient criterion. It is worth noticing also that the cooled and heated cases have the highest and lowest overshoot in the compressible skin-friction coefficient. However, they reach approximately the same plateau in the turbulent region. The incompressible skin-friction factor, on the other hand, shows the opposite behavior, where the cooled and heated cases have the minimum and maximum values of overshoot, respectively. It is found that the incompressible skin-friction coefficients closely follow the $C_{f,inc} = 0.074\sqrt{\rho_{aw}/\rho_w}\,\mathrm{Re}_x^{-0.2}$ in the fully turbulent region. These findings also agree with those reported in Hadjadj *et al.* (2015) for supersonic turbulent boundary layers with wall-heat transfer.

One reason for the aforementioned disagreement between LST and DNS might be due to the fact that the LST results use the self-similar boundary layer profiles for the cooled, adiabatic, and heated walls so they are in thermo-mechanical equilibrium; while in DNS all simulations start with the self-similar boundary layer profiles for the adiabatic condition, regardless of the wall temperature, which is imposed at $x = x_{in}$. Therefore, the DNS results might not be in thermo-mechanical equilibrium from the

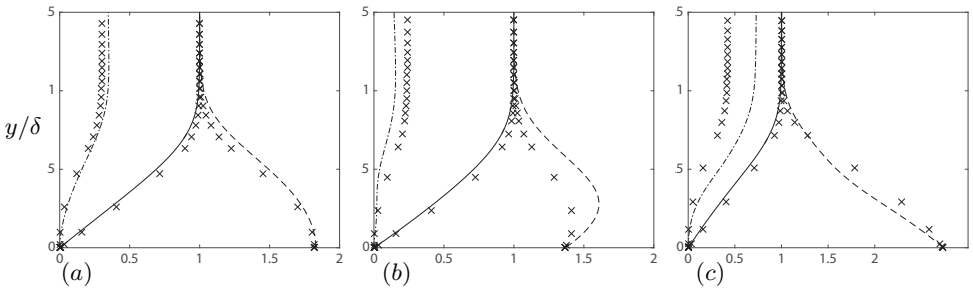

FIGURE 7. Comparison of flow mean profiles of (a) adiabatic (A1), (b) cooled (C1) and (c) heated (H1) walls at $\mathrm{Re}_x \approx 2.7\times10^6$ as a function of y/δ with their counterparts obtained from dedicated Blasius flow solver (MLL). ——, u/u_∞; $-\cdot-$, $[v/u_\infty]\times250$; - - -, T/T_∞, x (MLL).

beginning. Figure 7 shows the comparison of the mean flow profiles for all three wall temperatures at $\mathrm{Re}_x = 2.7\times10^6$ as a function of y/δ with their counterparts obtained from the self-similar boundary layer solution (MLL). It is seen that, unlike the adiabatic case in which mean profiles closely follow each other, the DNS results slightly deviate from their self-similar solution behaviors for heated and cooled cases, especially for the mean temperature profile.

The streamwise evolution of the shape factor $H = \delta^*/\theta$ and the total disturbance energy associated with unsteady streamwise velocity fluctuation $e(x) = \int \overline{u'_{rms}(x)}^2 dy$ are depicted in Figure 8. Here, δ^* and u'_{rms} are the displacement thickness and the root-mean-square (rms) streamwise velocity, respectively, averaged both in time and z-direction. At the inlet, the shape factor has a value of $H = 5.8$, which is identical to its counterpart calculated using the dedicated Blasius solver. After the perturbation strip, the shape factor behaves differently for either case. Whereas it is rather smooth for the adiabatic case, it has a sudden jump/drop for the heated/cooled case. Finally, it attains a minimum value before reaching a plateau in a fully turbulent region. The plateau has the value of $H = 3.54$, $H = 4.60$ and $H = 2.87$ at $\mathrm{Re}_\theta = 3000$ for adiabatic, heated and cooled walls, respectively. The same range of shape-factor values was previously reported by Shadloo *et al.* (2015) for fully turbulent supersonic boundary layers at $\mathrm{M}_\infty = 2.0$ and $\mathrm{Re}_\theta = 1820$ and for the same wall-boundary conditions.

Energy distribution, on the other hand, continuously evolves starting from the perturbation slot till its maximum value and is then dumped to its final fully turbulent level, which is approximately two orders of magnitude higher than its initial stage. Although the peak positions and magnitudes depend on the wall-heat transfer rate, the energy distribution in the fully turbulent region is the same for all cases regardless of the wall temperature.

4. Conclusions

Direct numerical simulations (DNS) for a laminar-to-turbulent transition in the presence of wall-heat transfer were performed. Supersonic boundary layers over a flat plate at $\mathrm{M}_\infty = 2.2$ were considered. Effects of disturbance amplitude and frequency, as well as wall temperature, were investigated. Results were compared against linear stability theory (LST). It was found that increasing the disturbance amplitude as well as perturbation frequency moves the transition upstream. The latter was also predicted by LST since the non-dimensional frequency F_{150} has higher growth rate than F_{75} does. Based

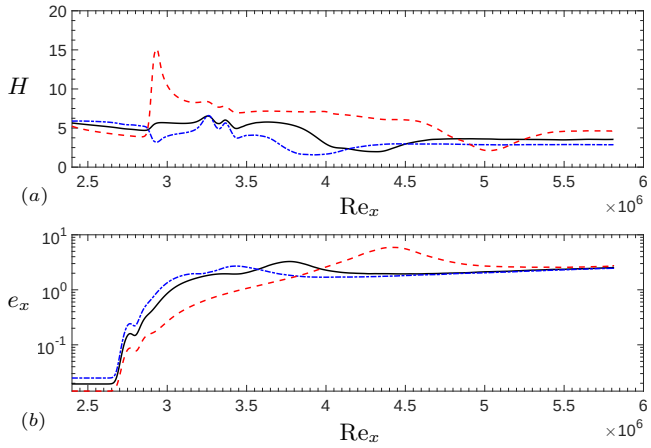

FIGURE 8. Streamwise evolution of (a) shape factor H and (b) disturbance energy e_x for DNS with —— adiabatic (A1), - - - heated (H1) and – · – cooled (C1) walls.

on the minimum skin-friction coefficient criterion, the transition location was found to be shifted downstream when the fluid is heated. Additionally, it was shown that the perturbation frequency and amplitude not only affect the transition length but also alter the maximum overshoot seen in the skin friction. The effect of wall-heat transfer was unforeseen. While the boundary layer instability region for the heated case was predicted to expand and has higher growth rates according to LST, the wall heating was seen to stabilize the flow and to postpone the transition. On the contrary, the simulations showed that the transition occurs at earlier Re_x for cooled, adiabatic and heated walls. One of the main reasons for this discrepancy could be the local effect of thermal non-equilibrium boundary layer on the transition.

Acknowledgments

This research is supported by the Center for Turbulence Research, Stanford University, during the 2016 Summer Program. The access to the French CRIANN (Centre Régional Informatique et d'Applications Numériques de Normandie) resources, under allocation 1998022, is acknowledged.

REFERENCES

ARNAL, D. & JUILLEN, J. 1978 *Contribution expérimentale à l'étude de la receptivité d'une couche limite laminaire à la turbulence de l'écoulement général.* ONERA Tech. Rep. #1/5018.

BEN-NASR, O., HADJADJ, A., CHAUDHURI, A. & SHADLOO, M. 2016 Assessment of subgrid-scale modeling for large-eddy simulation of a spatially-evolving compressible turbulent boundary layer. *Comput. Fluids.* (In Press).

BERNARDINI, M., PIROZZOLI, S. & ORLANDI, P. 2012 Compressibility effects on roughness-induced boundary layer transition. *Int. J. Heat Fluid Fl.* **35**, 45–51.

CEBECI, T. & SMITH, A. 1974 *Analysis of Turbulent Boundary Layers*. Academic Press, New York.

Chaudhuri, A., Hadjadj, A. & Chinnayya, A. 2011*a* On the use of immersed boundary methods for shock/obstacle interactions. *J. Comput. Phys.* **230**, 1731–1748.

Chaudhuri, A., Hadjadj, A., Chinnayya, A. & Palerm, S. 2011*b* Numerical study of compressible mixing layers using high-order WENO schemes. *J. Sci. Comput.* **47**, 170–197.

De Tullio, N., Paredes, P., Sandham, N. & Theofilis, V. 2013 Laminar–turbulent transition induced by a discrete roughness element in a supersonic boundary layer. *J. Fluid Mech.* **735**, 613–646.

Durbin, P. & Wu, X. 2007 Transition beneath vortical disturbances. *Annu. Rev. Fluid Mech.* **39**, 107–128.

Franko, K. J. & Lele, S. K. 2013 Breakdown mechanisms and heat transfer overshoot in hypersonic zero pressure gradient boundary layers. *J. Fluid Mech.* **730**, 491–532.

Hadjadj, A., Ben-Nasr, O., Shadloo, M. & Chaudhuri, A. 2015 Effect of wall temperature in supersonic turbulent boundary layers: A numerical study. *Int. J. Heat Mass Tran.* **81**, 426–438.

Jacobs, R. & Durbin, P. 2001 Simulations of bypass transition. *J. Fluid Mech.* **428**, 185–212.

Kendall, J. 1985 Experimental study of disturbances produced in a pre-transitional laminar boundary layer by weak freestream turbulence. *AIAA J.* **85**, 1965.

Klebanoff, P. 1971 Effect of free stream turbulence on a laminar boundary layer. *Bull. Am. Phys. Soc.* **16**, 203–216.

Matsubara, M. & Alfredsson, P. H. 2001 Disturbance growth in boundary layers subjected to free-stream turbulence. *J. Fluid Mech.* **430**, 149–168.

Pirozzoli, S., Grasso, F. & Gatski, T. 2004 Direct numerical simulation and analysis of a spatially evolving supersonic turbulent boundary layer at M= 2.25. *Phys. Fluids.* **16**, 530–545.

Redford, J. A., Sandham, N. D. & Roberts, G. T. 2010 Compressibility effects on boundary-layer transition induced by an isolated roughness element. *AIAA J.* **48**, 2818–2830.

Ryu, S., Marxen, O. & Iaccarino, G. 2015 A comparison of laminar-turbulent boundary-layer transitions induced by deterministic and random oblique waves at Mach 3. *Int. J. Heat Fluid Fl.* **56**, 218–232.

Sayadi, T., Hamman, C. W. & Moin, P. 2013 Direct numerical simulation of complete H-type and K-type transitions with implications for the dynamics of turbulent boundary layers. *J. Fluid Mech.* **724**, 480–509.

Schneider, S. P. 2008 Effects of roughness on hypersonic boundary-layer transition. *J. Spacecraft Rockets.* **45** (2), 193–209.

Schoppa, W. & Hussain, F. 2002 Coherent structure generation in near-wall turbulence. *J. Fluid Mech.* **453**, 57–108.

Shadloo, M., Hadjadj, A. & Chaudhuri, A. 2014 On the onset of postshock flow instabilities over concave surfaces. *Phys. Fluids.* **26**, 076101.

Shadloo, M., Hadjadj, A. & Hussain, F. 2015 Statistical behavior of supersonic turbulent boundary layers with heat transfer at M=2. *Int. J. Heat Fluid Fl.* **53**, 113–134.

Wu, X. & Moin, P. 2010 Transitional and turbulent boundary layer with heat transfer. *Phys. Fluids.* **22**, 085105.